

¹ Highlights

² **The Enceladian crater production function**

³ E. W. Wong, S. C. Werner, M. R. Kirchoff, R. Brasser

⁴ • Research highlight 1

⁵ • Research highlight 2

The Enceladian crater production function

E. W. Wong^{a,b,*}, S. C. Werner^c, M. R. Kirchoff^d, R. Brasser^{e,c}

^a*Geneva Observatory, University of Geneva, Chemin Pegasi 51, Versoix, CH-1290, Switzerland*

^b*Earth Life Science Institute, Tokyo Institute of Technology, Meguro-ku, Tokyo, 152-8550, Japan*

^c*Centre for Planetary Habitability, Department of Geosciences, University of Oslo, N-0315, Oslo, Norway*

^d*Southwest Research Institute, 1050 Walnut St, Suite 300, Boulder, CO, USA*

^e*Konkoly Observatory, HUN-REN CSFK, MTA Centre of Excellence, 15-17 Konkoly Thege Miklos St., H-1121, Budapest, Hungary*

14 Abstract

Conflicting perspectives on Enceladus' past and present interior state arise from predictions of its tidal history, and an uncertain prescription of its bombardment history, as well as limited interpretation of crater statistics. Here we present the first comprehensive global crater catalogue for Enceladus and build a crater production function from our dataset. The crater production function is the underlying, unmodified crater size-frequency distribution of the satellite surface, that is, it is the pristine size-frequency distribution that the craters would have assuming no subsequent modification. We obtained the function with a data-driven approach; therefore it makes no assumptions about the impactor source population (heliocentric versus planetocentric). The crater production function is therefore essential for computing surface ages when combined with a crater chronology function. We fit it with an 10th degree polynomial as is customary for the Moon and Mars, indicating the waviness at different crater diameters. Future work will indicate whether the Enceladian crater production function is unique or shared with the other nearby satellites.

Keywords:

1. Introduction

17 Enceladus, one of Saturn's regular, icy satellites, displays remarkable and ongoing geyser-like cryo-
 18 volcanism. Cassini's observations, such as the south pole's active degassing (Porco et al., 2004; Spencer
 19 et al., 2006) and physical libration (Thomas et al., 2016; Nimmo et al., 2023) provide strong, albeit indirect,
 20 evidence of a subsurface ocean (Porco et al., 2004; Spencer et al., 2006). Yet, the mechanisms sustaining
 21 its long-term internal activity remain unclear (Nimmo et al., 2023). Despite its small size and current low
 22 orbital eccentricity, the internal heat required to maintain this activity exceeds what is expected from tidal
 23 dissipation and radiogenic decay alone (Meyer and Wisdom, 2007; Roberts and Nimmo, 2008). Moreover,
 24 Enceladus' surface reveals a juxtaposition of both geologically young and ancient terrains.

26 In the absence of sample-return data for radiometric dating, crater counting serves as a primary tool for
 27 understanding the geological evolution of icy satellites like Enceladus. However, interpreting crater records
 28 remains challenging due to uncertainties surrounding the source, flux, and timing of impactors. Particularly
 29 for the Saturnian system, questions remain as to whether the dominant impactors are heliocentric comets

*Corresponding author

30 or system-internal debris. While planetocentric populations may have influenced some features (Ferguson
31 et al., 2022), the broad consensus is that heliocentric impactors, especially those originating from the scat-
32 tered disc, are the primary source of cratering across the outer solar system (Shoemaker and Wolfe, 1982;
33 Chapman and McKinnon, 1986; Zahnle et al., 1998; Nesvorný et al., 2019; Wong et al., 2023; Nesvorný
34 et al., 2023).

35
36 Against this background, our study introduces two key datasets and tools. First, a new crater production
37 function derived directly from Enceladus' observed crater record, independent of assumed impactor popu-
38 lation models. Second, the first global crater catalogue for Enceladus, based on a unified classification of
39 terrain units and crater morphologies.

40
41 These results are crucial for advancing data-driven methods in icy satellite studies. In particular, the
42 crater production function forms the foundational basis for future studies that aim to estimate surface ages
43 across Enceladus. While traditional age estimates have relied on imported or theoretical crater chronolo-
44 gies, our production function is explicitly anchored in the observed record, enabling a more reliable, body-
45 specific framework for later applications.

46
47 The detailed modelling of surface ages with an updated Enceladus-specific crater chronology will be
48 presented in a subsequent paper. Here, we quantify the spatial and size-frequency characteristics of craters
49 across all major surface units, in order to present a functional description for the crater size-frequency
50 distribution to provide a crater production function for Enceladus.

51 1.1. Terms and definitions

52 Craters form on the solid crust of the satellites. The term “*size-frequency distribution*” (abbreviated to
53 SFD) refers to a model of a statistical relationship between the diameters of craters and their frequency
54 of occurrence, which is express as spacial density (km^{-2}) for craters. Smaller craters are relatively more
55 abundant than larger craters, and therefore we could use power law expressions for the cumulative size-
56 frequency distribution is $n_{>D} \propto (D_0/D)^\alpha$, where D_0 is a scaling diameter in km, and α is the cumulative
57 slope for that size ranges. An older surface would typically have a higher crater density, which manifests as
58 an up-shifted distribution, assuming the same source and a specified rate of bombardment. The figures in
59 this paper show *size-frequency distributions* and *measurements* in cumulative frequency, where the number
60 of craters larger than a specific diameter is plotted against diameter, and the population decreases with in-
61 creasing size. We opted for cumulative distribution, because the observed undisturbed crater size frequency
62 distribution show a more complex shape than a single power law or a few broken power laws. In the later
63 section, we will use a polynomial description for the derived crater production function.

64 65 1.2. Crater production function

66 The crater production function (CPF) represents the underlying, unmodified crater size–frequency dis-
67 tribution on a planetary surface (Neukum et al., 1975). The CPF is presumed to remain unchanged over
68 time (Neukum et al., 1975; Neukum, 1983; Werner, 2014; Werner et al., 2023), forming the basis for crater-
69 based age estimates. Deviations between the actually observed crater size-frequency distribution and the
70 CPF, yields insight into the satellite's geological history, in particular when specific areas were (partially)
71 resurfaced. Although the assumption of a time-invariant CPF could be seen as a limitation, recent studies
72 suggest it is broadly valid: Bottke et al. (2024) found that the outer solar system projectile SFD stabilized
73 within ~ 40 Myr of planetesimal formation and has remained largely unchanged for the past 4.3 Ga (Bottke

74 et al., 2024).

75
76 Previous crater studies of Enceladus focused on specific terrains, particularly cratered plains, and in-
77 ferred projectile SFDs from three main sources: Jupiter-family comets, [Emi: check again] material ejected
78 from Triton, and Kuiper Belt objects (Zahnle et al., 2003; Singer et al., 2019; Bottke et al., 2024). However,
79 these SFDs were derived from different satellite systems (i.e., Jovian, Uranian and Pluto-Charon), where
80 variations in planetary encounter velocities and collision velocities with the satellites affect crater forma-
81 tion, limiting their direct applicability to Enceladus and the other Saturnian satellites.

82
83 These distributions (Fig. 1) mainly describe kilometre-scale projectiles, best constraints for large pro-
84 jectiles (e.g., >10 km). Yet, most observable craters on Enceladus, range from a few hundred metres to
85 34 km in diameter, which does not overlap in range where crater diameters are inferred. Given Enceladus'
86 low mass and the high impact velocities of heliocentric impactors (relative to other mid-sized Saturnian
87 satellites; Zahnle et al. 2003; Wong et al. 2021), most visible craters on Enceladus were formed by sub-
88 kilometre impactors. This is precisely the diameter range where the projectile population remains largely
89 unknown, making it unreliable for constructing a CPF.

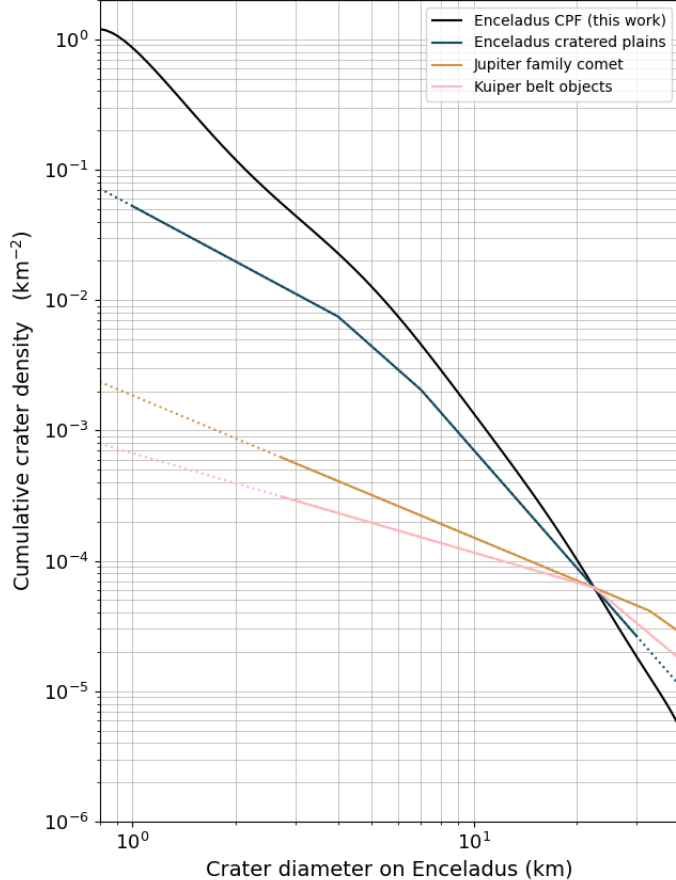


Figure 1: Enceladus crater production function and size-frequency distributions of craters and impactors in the outer Solar System. The displayed distributions include the Enceladus crater production function derived in this study (in black), the crater size-frequency distribution fitted from the trailing hemisphere mid-latitude crater plains (Kirchoff and Schenk (2009); in blue), the impactor size-frequency distribution resembling Jupiter-family comets (case A from Zahnle et al. (2003); in orange) and collisionally evolved population (case B from Zahnle et al. (2003); in mustard), and Kuiper belt objects (Singer et al. (2019); in red). The dashed lines indicate diameter ranges where the distribution was not covered in the reference data but was extended with the cumulative slope of the adjacent diameter ranges.

Previously, Wong et al. (2023) assumed an outer Solar System-wide crater production function derived from the Pluto-Charon craters (Singer et al., 2019, red line in Fig 1). However, such a distribution does not match that of Enceladus or the other Saturnian satellites of previous studies (Kirchoff et al., 2022, blue line)). Similarly, CPF constructed based on craters on other satellites in different systems, such as Ganymede, Callisto, and Europa (Zahnle et al., 2003, orange line), exhibit similar discrepancies (Wong et al., 2023). Consequently, no existing reference provides a CPF derived exclusively from data from Enceladus, prompting the need to construct one. The CPF resulting from the here presented work is shown in black in Fig 1.

100 **2. Data and Methods**

101 *2.1. First global crater survey on Enceladus*

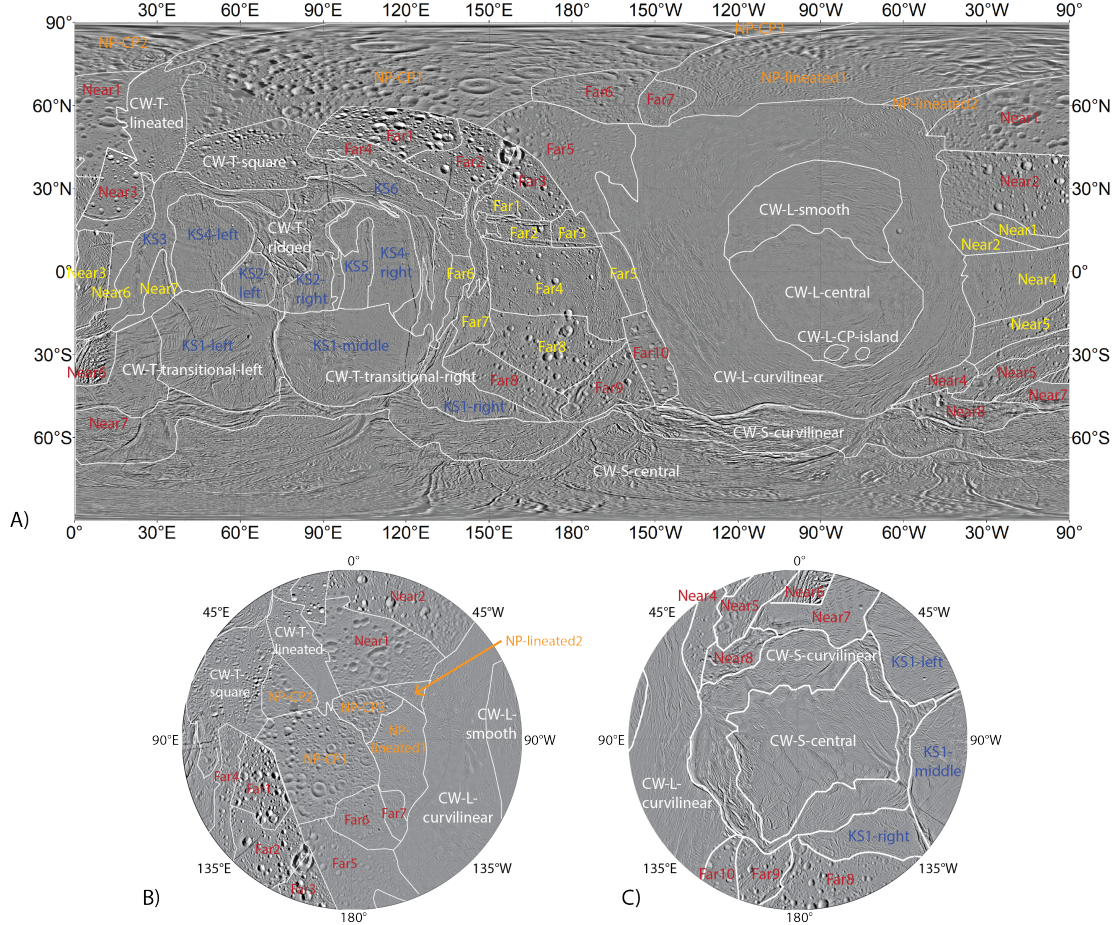


Figure 2: Division of geologic units on Enceladus. (A) in equirectangular projection from 60°S to 60°N , and (B) and (C) in polar stereographic from pole to 30° latitude in the north and south poles, respectively. Due to space constraints, not all units are labelled with full names. The prefix “RP” for ridged plains from Kirchoff and Schenk (2009) is omitted. Colour variations (red and yellow) distinguish between “Mid” (for mid-latitude) and “Eq” (for equator) without repeated labelling. Units in the north pole defined in this work are labelled in orange. Units referencing Kirchoff and Schenk (2009) are in blue, while those referencing Crow-Willard and Pappalardo (2015) are in white.

102 Crater counting is a subjective process whose outcomes vary among researchers (Robbins et al., 2014).
 103 To ensure reliability, this study independently conducted crater counts on Enceladus by E. Wong (EW) and
 104 M. Kirchoff (MK). EW surveyed craters from 50°S to 90°N , while MK covered from 90°S to 60°N , with an
 105 overlap at 50°S to 60°N (approximately 82% of Enceladus’ global area). Counts, where overlapping were
 106 cross-checked for statistical robustness. EW’s and MK’s set, no specific lower limit to identify craters; a

107 minimum cutoff at 800 m for EW and 1 km for MK is applied after surveying and recording all candidate
108 craters. The cut off is introduced for the entire survey of 16,958 craters. Using the global mosaic images
109 from Cassini released by Bland et al. (2018), due to variations in (camera) emission angles, (lighting) phase
110 angles, and image resolution among individual based images, we restrict our study to craters with diameters
111 larger than 800 m.

112
113 After compiling the global crater count, we divided Enceladus into 62 geological units as displayed in
114 Fig.2. These divisions are based on variations in terrain geomorphology, crater distribution, and instrumen-
115 tal image characteristics (see Sec. 2.3 for division criteria). Of these, 15 units, primarily on the leading
116 hemisphere and in the south polar region, are referenced from Crow-Willard and Pappalardo (2015), while
117 10 units, mainly in the trailing hemisphere's ridged plains, are adapted from Kirchoff and Schenk (2009).
118 The remaining units are newly delineated and proposed in this study.

119
120 *2.2. Details of crater survey*
121 EW's survey utilised the geodetically controlled global mosaic images released by Bland et al. (2018),
122 comprising 108 high-resolution images (55 to 419 m/pixel), with 96% of the total area below 200 m/pixel
123 resolution, and 18% below 100 m/pixel. Despite this, visual variations affect the minimum resolvable crater
124 diameter instrumentally. For instance, sub-kilometre craters are visible in mid-latitudes and equatorial re-
125 gions but harder to discern near the north pole due to lower resolution, despite similar expected crater
126 abundance based on the crater count at large diameter ranges and the region's proximity. Furthermore, the
127 solar incidence angle also affect crater identification (Ostrach et al., 2011), particular on the central leading
128 hemisphere, where low incidence angles shorten crater's shadow and reduce visibility.

129
130 MK's counts have been gathered for over a decade (2007–current) and have used the greyscale mosaics
131 generated by Paul Schenk throughout that time frame (Schenk et al., 2011, 2018) with the most recent being
132 published in Schenk and McKinnon (2024). Measurements were updated and added in both location and
133 diameter as cartography and imaging improved Kirchoff and Schenk (2016, 2018). As the images used in
134 the mosaic did not vastly differ from those used by Bland et al. (2018), similar issues affected MK's counts
135 as EW's counts discussed above.

136
137 EW employed ArcGIS with the CraterTools add-in (Kneissl et al., 2011) and QGIS with the OpenCrater-
138 Tool add-in (Heyer et al., 2023) to locate and document the diameter and coordinates of candidate craters.
139 MK employed both USGS ISIS (for only the earliest counts; Kirchoff and Schenk 2009) and JMARS
140 (<http://jmars.asu.edu/>; Christensen et al. 2009) to measure crater diameters and locations. In JMARS both
141 the 3-point crater counting and ellipse shape tools were used.

142 *2.3. Division of geological units*

143 This study's geologic unit divisions reference two earlier works: the global geomorphology studies by
144 Crow-Willard and Pappalardo (2015), and crater distribution studies focusing on the trailing hemisphere by
145 Kirchoff and Schenk (2009). Previous divisions have broadly treated certain regions as a single unit. For
146 instance, Crow-Willard and Pappalardo (2015) considers 320,000 km², or 41% of global Enceladus, as a
147 massive cratered plain. Even though Kirchoff and Schenk (2009) separated the anti-Saturn side cratered
148 plains into mid-latitude and equatorial cratered plains, both span wide areas and apparent differences exist
149 within these expansive cratered plains. Moreover, cratered plains on the Saturn-facing side hemisphere have
150 yet to be extensively studied. Combining surfaces with potentially varied solidification time and geological

151 histories, especially a younger surface with a lower crater density, dilutes the crater statistics that includes
152 mixed crater populations. This mixed population manifests in drops in incremental frequencies or shallowing
153 in cumulative frequencies given that smaller craters are more frequent than their larger counterparts,
154 resulting in a turnover or reduced slope in the SFD of small diameter ranges.

155
156 To ensure representative crater statistic and size-frequency measurements, vital for deciphering surface
157 ages and regional geological history, we divided Enceladus' entire surface into 62 geologic units based on
158 three criteria of difference: geomorphology, crater distribution, and instrumental image characteristics.

159 *2.3.1. First criterion: geomorphology*

160 Craters, being circular or elliptical, stand out prominently from most tectonic features, such as ridges,
161 troughs, and chasmata, which are often linear and parallel. However, challenges arise in distinguishing
162 craters from tectonic features of similar scales, particularly when the width of curvilinear troughs, as seen
163 in the transitional units (i.e., CW-T-transitional-left/right) defined by Crow-Willard and Pappalardo (2015),
164 resembles that of small craters (1 to 3.5 km wide). The cross-cutting troughs may produce quadrilateral
165 or circular-like features that mimic small craters. In cratered plains, heavily eroded "squarish" craters (see
166 Fig A.1) and craters intersected by pit chains (Fig A.3) can be challenging to discern and measure. The
167 size and shape of these questionable craters vary across geologic units due to differences in background
168 topography, requiring separate consideration of crater counts from each unit.

169
170 Ridges and troughs abound on Enceladus' younger surface form in large groups with similar widths
171 and run almost parallel, dominating specific regions such as the anti-Saturn side southern mid-latitude
172 cratered plain (Far-Eq-CP3) and the trailing hemisphere transitional plain (KS-RP1-middle). Identical ridge
173 or trough groups within a geologic unit suggest resurfacing by the same event, implying identical surface
174 ages and crater densities. Nevertheless, units with similar morphology might form at distinct times through
175 a similar process. Therefore, it is essential to consider the superimposed crater population as a criterion to
176 distinguish units that may appear similar, but have formed at different times.

177 *2.3.2. Second criterion: observable general crater distribution*

178 Crater density evidently varies across regions, even within the cratered plains and subdued cratered
179 plains defined by Crow-Willard and Pappalardo (2015). Calculating surface ages relies heavily on crater
180 density, as older surfaces accumulate more craters. Mixing crater counts from geologic units that solidified
181 at different times skews the average crater density and misrepresents solidification ages. Accurate age calcu-
182 lations necessitate bounding geologic units to areas with similar crater densities. However, Enceladus poses
183 specific challenges due to its complex and multiple resurfacing events because not all surfaces underwent
184 full resurfacing, where the entire crust melted and resolidified, erasing all pre-existing features, including
185 craters, and resetting ages. Instead, surfaces might be partially resurfaced. Some parts of the cratered plains
186 display a gradual decrease in crater density, such as from high to low latitudes (e.g., from Far-Eq-CP8 to
187 Far-Eq-CP4), or as surfaces approach the boundaries of crater terrains or specific tectonic features (e.g.,
188 Far-Eq-CP4~CP7). Overall, changes in crater density indicate variations in underlying surface ages, neces-
189 sitating the classification of distinct geologic units.

190
191 Manually drawing units' boundaries based on cumulative crater density could be arbitrary. Although
192 different studies define boundaries differently based on visually prominent surface morphologies, subdivi-
193 sion based on crater density as additional criterion avoids unrepresentative crater count interpretations and
194 will improves later age estimation.

195 2.3.3. *Third criterion: instrumental image characteristics*

196 Variations in the surface images of Enceladus affect crater counts and geomorphology identification. Im-
197 age resolution limits the minimal recoverable crater diameters and can artificially flatten the size-frequency
198 measurement as crater diameters approach the resolution limit. If a geological unit spans images with dif-
199 ferent resolutions, there will be a drop in the smaller crater count in part of the unit, creating an illusionary
200 flattening in the size-frequency measurement. To mitigate this, it is safer to separate such units.

201
202 Beyond resolution, illumination matters. Solar incidence angle — the angle between the incoming light
203 direction and the surface perpendicular line — influences shadow length and visibility. Higher incidence
204 angles result in longer, more pronounced shadows, revealing details such as crater wall shadows. Lower
205 incidence angles, typical at noon, produce uniform illumination, making it difficult to discern surface ir-
206 regularities and small-scale topography like relaxed craters and linear ridges/troughs with slighter elevation
207 changes.

208
209 Viewing geometry adds further constraints. Emission angle is the angle between Cassini's camera view-
210 ing direction and the surface perpendicular line. At high emission angles, features become distorted and size
211 measurement accuracy (e.g., width of ridges/trough and crater size) may be inaccurate. For visual examples
212 of appearance changes due to different incidence and emission angles, refer to Fig. 2 in Bland et al. (2018).

213
214 Variations in imaging conditions inherently yield diverse observed crater density and size-frequency
215 measurements. Combining crater counts across images may render crater density and size-frequency mea-
216 surements unrepresentative of the actual surface ages and geological history.

217
218 Shown in Fig 2, Enceladus is divided into 62 geologic units. Those that have been designated by
219 Crow-Willard and Pappalardo (2015) are prefaced with "CW", those by Kirchoff and Schenk (2009) with
220 "KS", and followed by location indicators: "T" for trailing hemisphere, or "L" for leading hemisphere.
221 The newly defined units in this work, mostly the cratered plains, are prefaced with "Far" and "Near" to
222 denote their locations on Enceladus' Saturn-facing and anti-Saturn sides, respectively, followed by "Mid"
223 for mid-latitude or "Eq" for equatorial region. North polar regions are prefaced with "NP" followed by
224 "CP" or "lineated" for crater plains and lineated plain, respectively. For the south polar region, we follow
225 those previously defined by Crow-Willard and Pappalardo (2015), thus the south polar curvilinear plains
226 (CW-S-curvilinear) and central plain (CW-S-central).

227 **Emi: Shall we still list all the geological unit, their full name, rough central coordinate and number of
228 crater counted on that unit?**

229 Here we like to remind the reader that, while a geologic unit typically denotes a distinct surface area
230 with similar formation, composition, age, and geological history, the term "geologic unit" in this study
231 may not precisely adhere to this definition due to its division based on image disparities, in addition to
232 geomorphology and crater distribution. Consequently, two units adjacent may form a geological unit, but
233 have been photographed at different resolutions and cannot be merged for the crater statistical assessment.

234 **SW: you could if you want add your geological map (the colored one you used before) which will be
235 used in the next article for deriving surface ages and the evolution of Enceladus.**

236 2.4. *Preparing crater counts to derive the Enceladus-specific crater production function*

237 Tectonic activities are hypothesised to selectively remove smaller craters while leaving larger ones rel-
238 atively intact (Michael and Neukum, 2010). Consequently, the observed crater size-frequency distribution

239 (SFD) gradually, and possibly irregularly, rolls off towards the smaller end, leading to a missinterpretation of
240 the crater production. Assessment of such mixed crater populations by including the smaller craters range
241 will underrepresent the original projectile flux, and thus the crater production function (CPF).

242 After acquiring the global crater database, we analysed it alongside surface morphology to assess how
243 tectonic resurfacing alters the crater SFD. In particular, we examined craters with diameters comparable to
244 the size of tectonic features that traverse the same terrain or those susceptible to be removed by partial resur-
245 facing, often extending from adjacent, younger terrains. This analysis allowed us to identify the minimum
246 crater diameter that remains largely unaffected by geological activity, which varies by region, typically from
247 1 km to 5 km. In heavily cratered regions, small craters are preferentially erased by subsequent impacts,
248 flattening the slope at the small end of the SFD. In tectonically active areas, ridges and troughs obscure or
249 erase craters of similar or smaller size. Conversely, in smoother, recently resurfaced terrains, newly formed
250 smaller craters could be distinguishable, with some preserved down to 1 km. Establishing this threshold
251 diameter enables the construction of an initial, non-geologically modified crater SFD, which serves as a
252 basis for the derivation of the CPF.

253
254 Not all identified map units were well suited to assess the undisturbed production distribution using the
255 observed crater SFDs. Table 1 lists the unit names, centers coordinates, number of craters and the con-
256 sidered crater diameter range. These allowed us to derive the CPF for the range between 800 m to 35 km
257 in crater diameter, encompassing the minimum resolvable diameter to the maximum one. To explore the
258 entire range, we used these 13 representative geologic units to cover the different diameter categories (see
259 Fig.3A). For the smaller craters (<3 km), we focused on sparsely cratered smooth plains devoid of large
260 impacts to minimise the risk of removal or contamination by secondary craters. For rarer large craters (>10
261 km), we utilised measurements from heavily cratered terrains, where more craters have accumulated, to
262 ensure statistical accuracy across expansive areas.

263
264 In Figure 3B, we illustrate the observed size-frequency measurements of the 13 representative geologic
265 unit (as listed in Table 1). The measurements are plotted, binned logarithmically in crater diameter with
266 a width of 0.05. Some units exhibit a large amounts of craters spanning a wider diameter ranges, while
267 certain smaller units are combined for a broader search area and larger statistical base to derive the function
268 at larger crater ranges. To enhance statistics, ideally all diameter ranges should be represented by several
269 measurements from various units. However, measurements are based on regions with different image reso-
270 lutions (see Fig. 12 of Bland et al. 2018), degrees of resurfacing, and post-impact modifications, allowing
271 only a limited accurate or representative crater size range. Therefore, we considered the largest possible
272 overlap of individual measurements to minimise statistical uncertainties and avoid gaps.

273
274 Fig. 3C showcases the same data as in Fig. 3B, with the arrows indicating by how much the crater
275 density at sparsely cratered geological units have to be up-scaled to align with those at the heavily cratered
276 units. The resulting CPF's profile when all crater measurements are aligned against a reference crater dis-
277 tribution is shown in Fig. 3D. We chose the “Far-Mid-CP5” terrain for its broad range of crater diameters
278 and intermediate crater density. To normalise the measurements of the other 12 representative geological
279 units, we determined the vertical scaling factor by averaging the ratio of crater frequencies within the diam-
280 eter range where the crater measurements overlap and show the best agreement. This approach follows the
281 methodology used for the lunar CPFs, both in the historical work of Neukum et al. (1975) and the recent
282 study by Xiao et al. (2024). Once aligned, the crater size-frequency measurements from the representative
283 geologic units with different crater densities were standardised and combined, forming a representative set

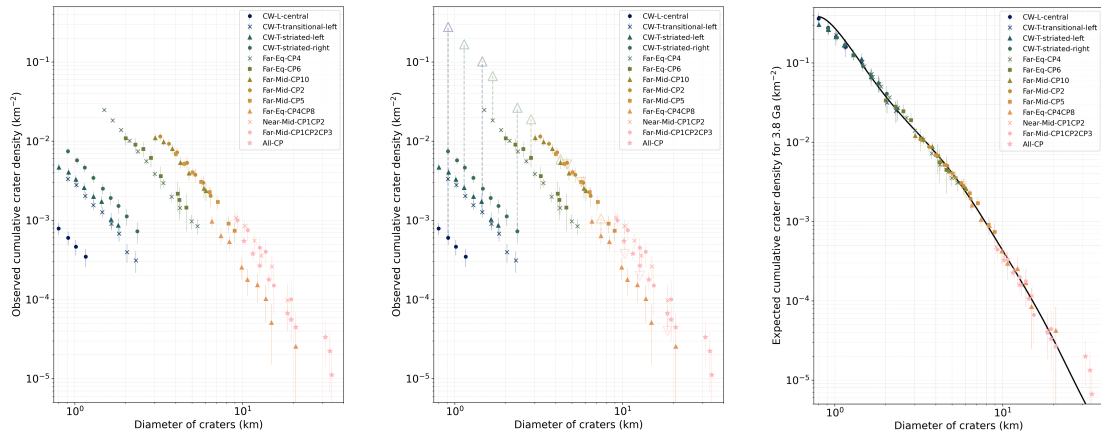
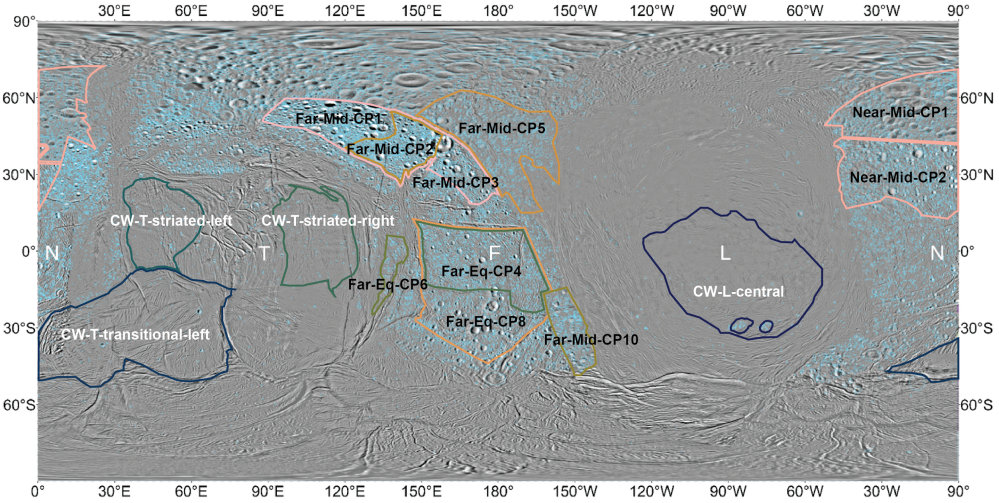


Figure 3: Construction of the crater production function (CPF). **(A)** Representative geological units overlaid on global mosaic images of Enceladus. White names denote units referenced from Kirchoff & Schenk (2017) and Crow-Willard & Pappalardo (2018), while black names denote units defined in this study. **(B)** Crater size-frequency measurements for each unit with logarithmic binning at 0.05 intervals. Transitioning colours (navy to pink) indicate increasing crater density and larger typical diameters. The error bars represent Poisson errors. **(C)** Visualisation of the upscaling and alignment of the crater measurements. **(D)** Normalised size-frequency measurements relative to the crater density of Far-Mid-CP5, with the black line shows a 10th-degree polynomial fit for the CPF.

284 of SFDs to trace the CPF (black line in Fig. 3D).

285

286 3. Results

287 3.1. Global crater distribution

288 Enceladus' craters are heterogeneously distributed across its icy surface. As depicted in Figure 4A, the
289 northern high latitude region (beyond 40°N) and in longitudinal direction narrow regions along the Saturn-
290 facing side (0°) and anti-Saturn side (180°) are densely cratered. Additionally, clusters of craters, such as

Geologic Unit	Lat., Long. ($^{\circ}$)	No. Craters	Fitting	Diameter Range (km)
CW-L-central	90°W, 10°S	34		0.8~1.5
CW-T-transitional-left	35°E, 30°S	125		0.9~2.5
CW-T-striated-left	50°E, 10°N	86		0.8~2.2
CW-T-striated-right	110°E, 5°N	120		0.9~2.5
Far-Eq-CP4	175°E, 30°S	1576		1.5~14
Far-Eq-CP6	137°E, 10°S	125		2.0~5.0
Far-Mid-CP3	166°W, 30°N	436		3.5~32
Near-Mid-CP2	18°E, 14°N	1450		5.0~15
Far-Mid-CP10	152°W, 30°S	338		3.0~7.0
Far-Mid-CP5	180°W, 40°N	813		4.0~10
Far-Mid-CP2	142°W, 42°N	579		3.2~32
Far-Eq-CP8	175°E, 30°S	857		4.3~21
Far-Mid-CP1	115°W, 50°N	638		4.0~16
Near-Mid-CP1	32°E, 12°N	1138		4.0~35

Table 1: List of the representative geologic units used to derive the crater production function. From left to right are the name codes, rough coordinates of the centre of the unit, number of crater counted within the unit, and the crater diameter ranges (in km) used to fit and scale for the crater production function. The ages are in billion years old (Ga) unless specified in million years old (Ma).

291 those around 80°W, 30°S; and 30°E, 0°, are observed within the more expansive yet scarcely cratered leading-
 292 and trailing hemispheres. The heterogeneity in the crater distribution is attributed to regional resurfacing
 293 of the icy crust, which has erased previous impact records, rather than being caused by preferential impact
 294 at specific locations on the satellite, i.e. the apex-antapex impact asymmetry (e.g. Ćuk et al. 2016). For
 295 further discussion on crater heterogeneity, see Sec. 4.3.

296
 297 Figure 4B compares the observed crater SFD across different geologic units on Enceladus. Each unit
 298 has a SFD that can be approximate by power laws. The SFD slope changes from one unit to another. Among
 299 the less densely cratered units (green and blue curves) the slopes are very similar [shall I add?:] and nearly
 300 parallel to the crater production function which is normlised to the global average crater density of
 301 ≥ 1 km craters. Conversely, the two SFDs for the most densely cratered units (orange and pink) differ from
 302 each other and exhibit a gradual decrease (roll-off) at distinct diameters (around 3~4 km). This roll-off and
 303 its implications are discussed in Sec. 4.1.

304
 305 *3.2. Fitting of the crater production function*

306 The crater production function for Mercury (Neukum et al., 2001), Mars (Ivanov et al., 2001; Hartmann,
 307 2005), and asteroids: Vesta, Ida (Schmedemann et al., 2014), and Ceres (Hiesinger et al., 2016), have been
 308 derived by fitting a mathematical function to the normalised crater SFDs, typically using polynomials or
 309 piecewise power laws. The former has traditionally been used for the lunar CPF (e.g., Neukum et al. 2001),
 310 while the latter is more common for describing impactor distributions in the outer Solar System (e.g., Zahnle
 311 et al. 2003). These empirical functions enable the translation of crater densities across different size ranges.

312
 313 For Enceladus, we derived a cumulative CPF by fitting the normalised and combined SFD (coloured

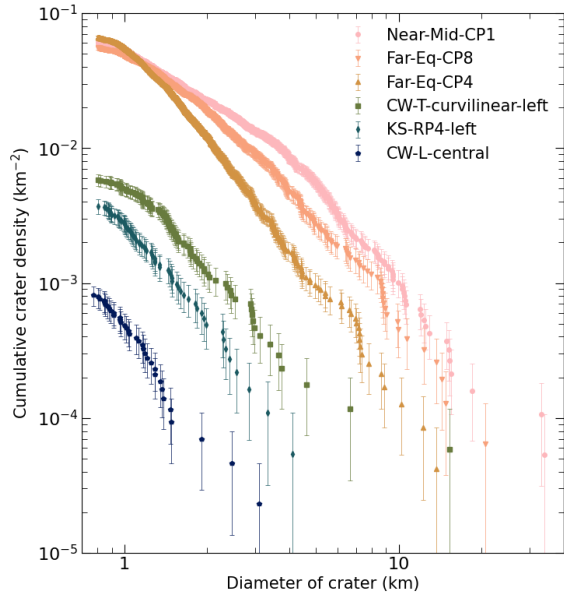
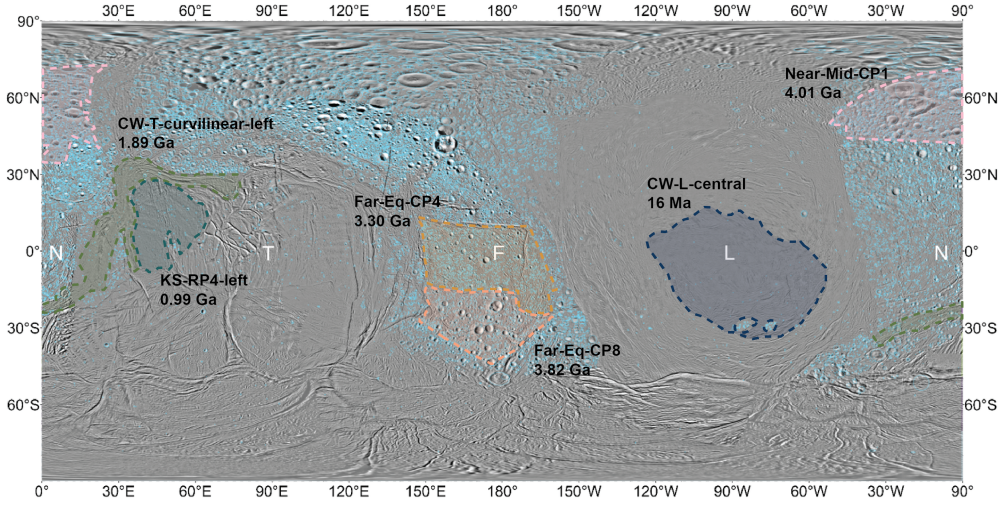


Figure 4: Demonstration of different crater populations across six geological units. **(A)** [Remove the ages] Cyan elliptical outlines highlight the uneven distribution of craters across Enceladus. Thin dashed lines bounding the semi-transparent areas mark the six distinctive geological units, each labelled with its name and best-fitted crater retention ages. Capital letters along the equator (N, T, F, L) represent the Near-side, Trailing, Far-side, and Leading hemispheres, aiding in unit location reference. **(B)** Raw and unbinned crater size-frequency measurements in cumulative distribution for the six geological units, with colours matching those in (A). Error bars represent Poisson errors. Differences in slope reflect variations in location and resurfacing degree. The six units were chosen to minimise partially resurfacing effects that obscure slopes.

314 points in Fig. 3D), we found that a 10th-degree polynomial (black line) best represents the CPF over crater
 315 diameters between 800 m and 35 km, while preserving a continuous downward slope.

316 To avoid unphysical absolute values, we express the polynomial fit of CPF in a *normalised form*, scaled
 317

Polynomial degree n	Coefficient a_n
0	-0.0653
1	-2.3503
2	-5.5573
3	24.951
4	-77.268
5	212.99
6	-406.68
7	464.58
8	-303.37
9	104.74
10	-14.850

Table 2: Coefficients of the polynomial representation of Enceladus’ cumulative crater production function. The polynomial describes the relative shape of the cumulative distribution; absolute normalisation is defined separately.

318 to the cumulative crater densities expected from a typical 1 km projectile (i.e., heliocentric comet) on Enceladus. This corresponds to a final crater diameter of $D_{\text{cr}} = 22.6 \text{ km}$, derived from icy–satellite crater scaling
 319 relations (e.g., Zahnle et al., 2003). The normalised CPF is expressed as:

$$\log \tilde{S}(D_{\text{cr}}) = \sum_{i=0}^{10} a_i [\log D_{\text{cr}}]^i, \quad (1)$$

321 where D_{cr} is crater diameter in km, $S(D_{\text{cr}})$ is a *dimensionless shape function* that describes the relative
 322 form of Enceladian cumulative crater density. This estimate is based on the currently known number of
 323 scattered disc objects larger than 10 km, $(2.0 \pm 0.8) \times 10^7$ (Nesvorný et al., 2019). The normalised function
 324 $\tilde{S}(D_{\text{cr}})$ is defined such that $\tilde{S}(D_{\text{ref}}) = 1$ at the reference diameter $D_{\text{ref}} = 22.6 \text{ km}$, which corresponds to
 325 the final crater size expected from a 1 km impactor on Enceladus (Zahnle et al., 2003; Wong et al., 2023).

326
 327 Table 2 lists the polynomial coefficients a_0 – a_{10} that include this normalisation, accounting for Enceladus’ impact probability (Wong et al., 2023; Brasser et al., 2025), Enceladus’ global surface area, and
 328 number of scattered disc objects mentioned above. However, a_0 obviously is changing depending on the
 329 actual crater density of the studied geological unit and is used as an relative age measure.

331
 332 It is important to note that $S(D_{\text{cr}})$ alone does not represent a physical crater density or cumulative
 333 number of craters. Instead, it provides a relative scaling with diameter. Physical quantities, e.g., expected
 334 crater densities, are obtained by normalising $S(D_{\text{cr}})$ at a reference diameter, such as that produced by a
 335 1 km comet. In this way, the polynomial captures the *shape* of the production function, while the absolute
 336 normalisation is set externally.

337
 338 For reproducibility and publication of our CPF, the Python code accompanying this study includes (i)
 339 the polynomial function of the CPF, (ii) functions to compute crater densities for arbitrary impactor diameters,
 340 and (iii) comparisons with other published impactor and crater SFDs. This implementation allows
 341 users to reproduce Fig. 1 and to adapt the CPF to updated satellites specific input parameters, e.g., different
 342 icy satellites’ surface gravity, impact velocities and impact probability, etc.

343 To facilitate comparison to a piecewise linear power-law fitting, where different crater diameter ranges
344 follow distinct power-law slopes, we note that the corresponding cumulative power-law slope of this poly-
345 nomial varies from -2.6 to -4.2. The slope is shallower below $D_{cr} \sim 3$ km and steepens beyond $D_{cr} \sim 7$ km,
346 although this transition is not pronounced enough to indicate a clear break in the SFD at 7–8 km. Such
347 steepening at the largest diameters likely reflects edge effects due to the rarity of large craters. For compari-
348 son, Kirchoff and Schenk (2009) reported cumulative slopes of -1.4 to -2.9 for smaller craters and -3.0
349 to -4.3 for craters larger than 7 km (see their Table 2). The slopes derived from our CPF fall comfortably
350 within this previously reported range.
351

352 We end with the following statement: CPF we present does not assume the projectile origin—heliocentric
353 or planetocentric—or their relative contributions, as the CPF is derived directly from crater counts rather
354 than model-based predictions. The diameter range piecewise overlap supports the underlying assumption
355 that the projectile population is similar through time.
356

357 4. Discussion

358 [SW: Write a small intro that now with a production function and geomorphological analysis of
359 the units you can start discussion Enceladus evolution models. currently the section starts out of nothing
360 and maybe also a bit to far from the main topic, because actually you will need timescales /rates
361 as a convincing line of arguments and that you cannot provide here ...]
362

363 4.1. Rolling-off of crater size-frequency distributions

364 From Fig. 4B, we observe that the two most heavily cratered terrains (orange and pink data) exhibit a
365 gradual decrease (roll-off) in crater frequency at smaller diameters ($\sim 3\text{--}4$ km). Similar roll-off also appear
366 in the size-frequency measurements of other heavily cratered units, i.e., CW-T-north-lineated, CW-T-square,
367 Far-Eq-CP8, Far-Mid-CP1, and all units in the north pole region (see App. ?? for the corresponding size-
368 frequency measurement of the units). This roll-off is not due to observational bias, as it occurs above the
369 resolution limit of the images used for crater identification. Instead, it likely results from geological pro-
370 cesses that have modified the original crater population.
371

372 One could argue this rolling-off results from a change in the cratering population with time. Yet, geo-
373 morphological analysis points towards partial resurfacing as a plausible and more straightforward explana-
374 tion, selectively removing small craters first, and most prominently for the heavily cratered plains (Michael
375 and Neukum, 2010). In heavily cratered regions, having accumulated high crater densities, must have so-
376 lidification earlier, but have since been intruded by tectonic-like structures extending from neighbouring
377 terrains. Newly formed craters suffered less erosion from ongoing tectonic and other resurfacing activities.
378 Cassini’s images reveal ample evidence of partially eroded or traversed craters within the ancient cratered
379 plains, affected by tectonic structures extending from neighbouring, less-cratered younger surfaces.
380

381 For example, in the trailing hemisphere, the relatively young CW-S-curvilinear unit—identified by its
382 well-preserved curvilinear ridges and scarcity of craters—has tranversed and eroded small craters along the
383 southern boundary of the heavily cratered Far-Mid-CP1 unit. Similarly, in the leading hemisphere, the for-
384 mation of the smooth and sparsely cratered terrain, CW-L-Curvilinear, apparently smoothed the craters
385 in nearby cratered plains, i.e., Near-Mid-CP1 and Near-Mid-CP2, producing ridged and lineated structures

386 that cut across pre-existing craters and preferentially removed smaller ones. Additional examples of partial
387 resurfacing, crater erosion, and tectonic-like modification are provided in the Appendix.

388
389 By contrast, scarcely cratered regions (e.g., Fig. 4B green and blue, units around the central leading
390 and trailing hemisphere) appear smoother and geomorphologically more homogeneous, often dominated by
391 single-directional lineated bands of ridges and troughs. Their low crater density suggests they formed more
392 recently, while their structural uniformity implies resurfacing occurred during a single, coherent geological
393 event. Having undergone fewer episodes of tectonic-like reworking and crater erosion, their crater popula-
394 tions are less modified. Consequently, the size-frequency distributions of these less-cratered and expected
395 to be more recently solidified terrains show little or no roll-off and align more closely with the CPF derived
396 in this study.

397
398 Another possible explanation for the roll-off is crater saturation. While our study does not advocate this
399 as the primary cause, it is worth considering its potential effects. In Fig. 4B, the two dashed lines mark
400 the 10% geometrically saturated crater density (N_{gs}) and 1% N_{gs} , thresholds where crater destruction and
401 production begin to balance, starting with smaller craters (?). On more heavily cratered terrains (pink and
402 orange data), the SFD rolls off at larger diameters, reflecting their longer exposure to impacts and approach
403 toward higher saturation levels. Moderately cratered terrains (e.g., yellow data) may have reached only mi-
404 nor saturation, with roll-offs beginning at smaller diameters as parts of their distributions fall within the 1%
405 N_{gs} regime. Despite these insights, ? cautions that conventional evaluation of equilibrium crater densities
406 may be unreliable: saturation may occur at even lower levels than 1% N_{gs} , and that local geology, initial
407 impactor SFD, and tectonic activity (prominent on Enceladus) play more dominant roles in shaping the
408 crater populations.

409
410 **4.2. Crater relaxation**
411 Recently Bland et al. (2012); Martin et al. (2023) indicate that Enceladus' low gravity, current heat
412 flux of < 40 to > 120 mW m⁻² (Čadek et al., 2019; Kinczyk et al., 2024), and surface temperature of
413 ~70 K make complete crater burial through viscous relaxation and burial by south polar plumes and E-ring
414 material alone unlikely. However, the observed crater relaxation (e.g., Bland et al. 2012) and scarcity of
415 large craters near the equator likely required a short period of excessive heat flux (>150 mW m⁻²) and
416 warmer subsurface temperatures (~150 K). Such condition, possibly enhanced by insulation from regolith
417 or plume material. Under a constant heat flux of 150 mW m⁻² on a 150 K surface, craters 15–20 km in
418 diameter with depth-to-diameter ratios of ~0.2 could relax by over 80%. Moreover, at a current maximum
419 equatorial deposition rate of ~10⁻³ mm yr⁻¹, these craters could be buried within few hundred million
420 years (Bland et al., 2012). Although a constant heat flux is unlikely, this relaxation timescale could still be
421 achieved with transient periods of extreme heat flux and higher deposition, e.g., due to shift in the locus of
422 plume activity (Bland et al., 2012). Ongoing work continues to refine models of historical and current heat
423 flux and deposition.

424 **4.3. Crater Heterogeneity on Enceladus**
425 Like many outer Solar System icy satellites, Enceladus is tidally locked, meaning its leading hemisphere
426 constantly faces the direction of its orbital motion. One would thus expect a crater apex-antapex asymmetry,
427 where the leading hemisphere experiences a higher cratering rate due to impacts from heliocentric ecliptic
428 comets.

429

430 However, our global crater distribution on Enceladus reveals a different pattern. Heavily cratered
431 regions are concentrated along the Saturn-facing (0° longitude) and anti-Saturn (180° longitude) hemispheres,
432 with the highest crater density located near the north pole. Our analysis for craters with diameters greater
433 than 1 km shows a leading-to-trailing hemisphere ratio (L/H) of 0.67, i.e., the leading hemisphere has a
434 lower crater count. This deviation from the expected asymmetry is also observed on other icy satellites,
435 such as Callisto, Ganymede, and Rhea, likely due to factors such as global crater saturation or impact ejecta
436 redistribution (Zahnle et al., 2003; Xu et al., 2017; Schenk et al., 2020). On Enceladus, the absence of the
437 expected crater asymmetry could be due to similar factors, or to periods of non-synchronous rotation or
438 resurfacing events that erased earlier cratering records.

439 *HERE** [SW: This comes out of the blue. You would need to introduce this in the method section.
440 Probably better to make actually three papers out of this!]. [Emi: move this to the result section and
441 briefly explain that we had also consider the expected cratering asymmetry.]

442 To investigate further, we conducted a dynamical N-body simulation of heliocentric comets and planetocentric
443 irregular satellites impacting Saturn's regular satellites, from Mimas to Titan (Wong et al., 2021). The
444 orbital elements of irregular satellites (planetocentric population) originate from Nesvorný et al. (2007).
445 Our simulation yielded L/H = 8.3 for heliocentric impacts and L/H = 29.3 for planetocentric impacts, sig-
446 nificantly higher than observed. These results rely on assumptions such as (i) constant synchronous rotation
447 since crustal solidification, (ii) no icy crustal drift despite the presence of a subsurface ocean, and (iii) no
448 regional resurfacing that erases the crater record. These assumptions are unrealistic, and their absence likely
449 explains the discrepancy between the expected and observed asymmetry on Enceladus. Such an experiment
450 was designed to test how extreme scenarios, like maintaining these assumptions, would affect the estimated
451 ages.

452 In the main text, cratering rates and crater densities are reported as global averages, calculated over
453 Enceladus' surface area of $\sim 790,000 \text{ km}^2$. Even considering an extreme apex-antapex asymmetry, our con-
454 clusion regarding Enceladus' ancient geological activity remains unchanged: for the most heavily cratered
455 terrain, with an estimated age of $\sim 4.1 \text{ Ga}$, adjusting for increased cratering on the leading side or decreased
456 cratering on the trailing side would only shift the age to be between 4.0 and 4.3 Ga. To further explore crater
457 heterogeneity on Enceladus, we reviewed the following key factors.

459 1) *Non-synchronous rotation*: Zahnle et al. (2001) suggested that satellites may not maintain syn-
460 chronous rotation over geological time based on Monte Carlo simulations of comet impacts (on the cur-
461 rently known synchronously rotating satellites). Evidence from Europa, a Galilean satellite, indicates non-
462 synchronous rotation or ice shell migration decoupled from the subsurface ocean (Kattenhorn and Hurford,
463 2009; Collins and Nimmo, 2009). While this could apply to Enceladus, the literature lacks clarity on when
464 or how synchronous rotation might have been disrupted. Therefore, we refrain from incorporating this into
466 our model.

467 2) *Icy crustal drift*: Martin and Kattenhorn (2014) inferred that Enceladus' ice crust had rotated at
468 least 115° based on pit chain formations around the Southern equator to mid-latitude regions. Given the
469 concentration of heavily cratered terrain around the north pole, significant crustal migration, such as po-
470 lar wander, would require the original leading hemisphere to rotate by $\sim 90^\circ$ along the rotational axis.
471 While giant impacts or gravitational anomalies could have contributed to such shifts, evidence is lacking.
472 Surveys of crustal thickness or thermal anomalies (e.g., Schenk and McKinnon 2024) could offer further
473 insights, but current data do not support large-scale crustal reorientation as the cause of crater heterogeneity.

475

476 3) *Regional resurfacing*: We argue that regional resurfacing provides the most plausible explanation for
 477 the lack of crater asymmetry, as also proposed by Zahnle et al. (2001). Evidence from our global crater
 478 counts and geomorphological analysis supports resurfacing events at the south pole, Leading Hemisphere,
 479 and Trailing Hemisphere. This was also raised by Patterson et al. (2018), who described that the currently
 480 observed heavily cratered regions around the north pole and along 0° (central longitude of the Saturn-facing
 481 side) and 180° (central longitude of the anti-Saturn side), correspond to the areas left over after the forma-
 482 tion of geologically younger terrains of south pole, leading hemisphere, and trailing hemisphere. Patterson
 483 et al. (2018) further proposed that prior to resurfacing, the cratered plains might have covered a more exten-
 484 sive area, potentially global in extent.

485

486 Resurfacing events could have erased any pre-existing crater asymmetry. Notably, central geological
 487 units in the leading hemisphere exhibit low crater densities, consistent with relatively recent resurfacing;
 488 the exact timing will be discussed in a future publication. Additionally, Enceladus orbits within Saturn's E-
 489 ring could offer an external explanation for the reduced crater count on its leading side. As it plows through
 490 the ring, the leading hemisphere may collect more E-ring ice particles, gradually mantling and obscuring
 491 crater, which makes the surface appear smoother than the trailing side.

492

493 In summary, the observed crater heterogeneity on Enceladus is likely due to a combination of resur-
 494 facing events and potential external factors, i.e., infall E-ring material, rather than an asymmetry in the
 495 bombardment rate. In future works we shall apply the CPF to compute the global activity history of Ence-
 496 ladus.

497 5. Conclusions

498 In this work, we have derived what is known to us to be the first CPF of an outer Solar System icy
 499 satellite. The CPF is the underlying, unmodified crater SFD of the satellite surface; that is, it is the pristine
 500 SFD that the craters would have, assuming no subsequent modification. The CPF is therefore essential
 501 for computing surface ages when combined with a crater chronology function. For this work EW and MK
 502 counted a combined 16958 craters on the Enceladian surface to compute the CPF, which was fit with an 10^{th}
 503 degree polynomial as is customary for the Moon and Mars (Neukum et al., 1975, 2001; Ivanov et al., 2001).
 504 The resulting crater size-frequency distribution is overall steeper than implied by previous assessments
 505 of the projectile population. The steep slope persists across Enceladus' geological record, indicating that
 506 the steepness is not primarily the product of extensive secondary cratering, and further implies that the
 507 crater-forming projectile population has not undergone any recognizable change through time. Future work
 508 will indicate whether the Enceladian CPF can be applied to the other Saturnian satellites, or whether it
 509 is unique. Either result would yield greater insight into the source populations responsible for satellite
 510 bombardment in the Saturnian system. With an appropriate description of the projectile flux, it will also
 511 be possible to constrain the timing and rates of the processes that modified Enceladus' surface. In this
 512 contribution, however, we focus on describing the nature and sequence of these processes. Importantly,
 513 Enceladus' surface evolution reflects the combined influence of endogenic activity—driven primarily by
 514 tidal heating—and exogenic modification through impact cratering. Together, these mechanisms rejuvenate
 515 the surface, obscuring or erasing parts of its cratering record while preserving clues to the moon's complex
 516 (and potentially ancient) geological history.

517 **Acknowledgments**

518 To prevent visual distortion of the data and exclusion of readers with colour-vision deficiencies, the
519 Scientific colour map below Crameri et al. (2020) is used in all the figures in this work. EW would like
520 to thank the Japan Society for the Promotion of Science (JSPS) for the support provided through the JSPS
521 Research Fellow grant No. 22KJ12886. SCW and RB acknowledge the Research Council of Norway for
522 funding through its Centres of Excellence funding scheme, project No. 332523 PHAB. MRK appreciates
523 the support from the NASA Cassini Data Analysis Program, grant No. 80NSSC22K0632. Our QGIS map
524 with complete crater counts and geological units are available by email request from the corresponding au-
525 thor.

526

527 **References**

- 528 Bland, M.T., Becker, T.L., Edmundson, K.L., Roatsch, T., Archinal, B.A., Takir, D., Patterson, G.W.,
529 Collins, G.C., Schenk, P.M., Pappalardo, R.T., Cook, D.A., 2018. A New Enceladus Global Control
530 Network, Image Mosaic, and Updated Pointing Kernels From Cassini's 13-Year Mission. *Earth and*
531 *Space Science* 5, 604–621.
- 532 Bland, M.T., Singer, K.N., McKinnon, W.B., Schenk, P.M., 2012. Enceladus' extreme heat flux as revealed
533 by its relaxed craters. *Geophysical Research Letters* 39, 17.
- 534 Bottke, W.F., Vokrouhlický, D., Nesvorný, D., Marschall, R., Morbidelli, A., Deienno, R., Marchi, S.,
535 Kirchoff, M., Dones, L., Levison, H.F., 2024. The Bombardment History of the Giant Planet Satellites.
536 *PSJ* 5, 88. doi:10.3847/PSJ/ad29f4.
- 537 Brasser, R., Wong, E.W., Werner, S.C., 2025. The current impact rate on the regular satellites of Jupiter,
538 Saturn, and Uranus. 695, A276. doi:10.1051/0004-6361/202453433.
- 539 Chapman, C.R., McKinnon, W.B., 1986. Cratering of planetary satellites., in: Burns, J.A., Matthews, M.S.
540 (Eds.), IAU Colloq. 77: Some Background about Satellites, pp. 492–580.
- 541 Christensen, P.R., Engle, E., Anwar, S., Dickenshied, S., Noss, D., Gorelick, N., Weiss-Malik, M., 2009.
542 JMARS - A Planetary GIS, in: AGU Fall Meeting Abstracts.
- 543 Collins, G., Nimmo, F., 2009. Chaotic Terrain on Europa, in: Pappalardo, R.T., McKinnon, W.B., Khurana,
544 K.K. (Eds.), *Europa*, p. 259.
- 545 Crameri, F., Shephard, G.E., Heron, P.J., 2020. The misuse of colour in science communication. *Nature*
546 *Communications* 11, 5444.
- 547 Crow-Willard, E.N., Pappalardo, R.T., 2015. Structural mapping of Enceladus and implications for forma-
548 tion of tectonized regions. *Journal of Geophysical Research Planets* 120, 928–950.
- 549 Ferguson, S.N., Rhoden, A.R., Kirchoff, M.R., Salmon, J.J., 2022. A unique Saturnian impactor population
550 from elliptical craters. *Earth and Planetary Science Letters* 593, 117652. doi:10.1016/j.epsl.2022.117652.
- 551 Hartmann, W.K., 2005. Martian cratering 8: Isochron refinement and the chronology of Mars. *Icarus* 174,
552 294–320. doi:10.1016/j.icarus.2004.11.023.

- 553 Heyer, T., Iqbal, W., Oetting, A., Hiesinger, H., van der Bogert, C.H., Schmedemann, N., 2023. A comparative analysis of global lunar crater catalogs using OpenCraterTool - An open source tool to determine
554 and compare crater size-frequency measurements. *Planetary and Space Science* 231, 105687.
- 556 Hiesinger, H., Marchi, S., Schmedemann, N., Schenk, P., Pasckert, J.H., Neesemann, A., O'Brien, D.P.,
557 Kneissl, T., Ermakov, A.I., Fu, R.R., Bland, M.T., Nathues, A., Platz, T., Williams, D.A., Jaumann, R.,
558 Castillo-Rogez, J.C., Ruesch, O., Schmidt, B., Park, R.S., Preusker, F., Buczkowski, D.L., Russell, C.T.,
559 Raymond, C.A., 2016. Cratering on Ceres: Implications for its crust and evolution. *Science* 353, aaf4758.
560 doi:10.1126/science.aaf4759.
- 561 Ivanov, B.A., Neukum, G., Wagner, R., 2001. Size-frequency distributions of planetary impact craters and
562 asteroids. volume 261. pp. 1–34.
- 563 Kattenhorn, S.A., Hurford, T., 2009. Tectonics of Europa, in: Pappalardo, R.T., McKinnon, W.B., Khurana,
564 K.K. (Eds.), *Europa*, p. 199.
- 565 Kinczyk, M.J., Byrne, P.K., Patterson, G.W., 2024. The Geological History of Enceladus' Cratered Terrains.
566 *Journal of Geophysical Research (Planets)* 129.
- 567 Kirchoff, M., Schenk, P.M., 2018. Enceladus' Expanded Impact Crater Database, in: AAS/Division for
568 Planetary Sciences Meeting Abstracts 50, p. 415.07.
- 569 Kirchoff, M.R., Dones, L., Singer, K., Schenk, P., 2022. Crater Distributions of Uranus's Mid-sized Satel-
570 lites and Implications for Outer Solar System Bombardment. *PSJ* 3, 42.
- 571 Kirchoff, M.R., Schenk, P., 2009. Crater modification and geologic activity in Enceladus' heavily cratered
572 plains: Evidence from the impact crater distribution. *Icarus* 202, 656–668.
- 573 Kirchoff, M.R., Schenk, P., 2016. Expanding Enceladus' Impact Crater Database, in: AGU Fall Meeting
574 Abstracts, pp. P33A-2124.
- 575 Kneissl, T., van Gasselt, S., Neukum, G., 2011. Map-projection-independent crater size-frequency de-
576 termination in GIS environments—New software tool for ArcGIS. *Planetary and Space Science* 59,
577 1243–1254.
- 578 Martin, E.S., Kattenhorn, S.A., 2014. A History of Pit Chain Formation Within Enceladus' Cratered Ter-
579 rains Suggests a Nonsynchronous Rotation Stress Field, in: 45th Annual Lunar and Planetary Science
580 Conference, p. 1083.
- 581 Martin, E.S., Whitten, J.L., Kattenhorn, S.A., Collins, G.C., Southworth, B.S., Wiser, L.S., Prindle, S.,
582 2023. Measurements of regolith thicknesses on Enceladus: Uncovering the record of plume activity.
583 *Icarus* 392, 115369.
- 584 Meyer, J., Wisdom, J., 2007. Tidal heating in Enceladus. *Icarus* 188, 535–539.
- 585 Michael, G.G., Neukum, G., 2010. Planetary surface dating from crater size-frequency distribution mea-
586 surements: Partial resurfacing events and statistical age uncertainty. *Earth and Planetary Science Letters*
587 294, 223–229.
- 588 Nesvorný, D., Vokrouhlický, D., Morbidelli, A., 2007. Capture of Irregular Satellites during Planetary
589 Encounters. *AJ* 133, 1962–1976.

- 590 Nesvorný, D., Vokrouhlický, D., Stern, A.S., Davidsson, B., Bannister, M.T., Volk, K., Chen, Y.T., Gladman, B.J., Kavelaars, J.J., Petit, J.M., Gwyn, S.D.J., Alexandersen, M., 2019. OSSOS. XIX. Testing Early
591 Solar System Dynamical Models Using OSSOS Centaur Detections. *AJ* 158, 132. doi:10.3847/1538-
592 3881/ab3651, arXiv:1907.10723.
- 594 Nesvorný, D., Dones, L., De Prá, M., Womack, M., Zahnle, K.J., 2023. Impact Rates in the Outer Solar
595 System. *The Planetary Science Journal* 4, 139.
- 596 Neukum, G., 1983. Variations in Crater Size Distributions: Implications for the Meteoroid Complex. *Meteoritics* 18, 362.
- 598 Neukum, G., Ivanov, B.A., Hartmann, W.K., 2001. Cratering Records in the Inner Solar System in Relation
599 to the Lunar Reference System. *Space Science Reviews* 96, 55–86.
- 600 Neukum, G., Koenig, B., Fechtig, H., Storzer, D., 1975. Cratering in the earth-moon system: consequences
601 for age determination by crater counting, in: *Lunar and Planetary Science Conference Proceedings*, pp.
602 2597–2620.
- 603 Nimmo, F., Neveu, M., Howett, C., 2023. Origin and Evolution of Enceladus's Tidal Dissipation. *Space
604 Science Reviews* 219, 57.
- 605 Ostrach, L.R., Robinson, M.S., Denevi, B.W., Thomas, P.C., 2011. Effects of Incidence Angle on Crater
606 Counting Observations, in: *42nd Annual Lunar and Planetary Science Conference*, p. 1202.
- 607 Patterson, G.W., Kattenhorn, S.A., Helfenstein, P., Collins, G.C., Pappalardo, R.T., 2018. The Geology of
608 Enceladus, in: Schenk, P.M., Clark, R.N., Howett, C.J.A., Verbiscer, A.J., Waite, J.H. (Eds.), *Enceladus
609 and the Icy Moons of Saturn*, p. 95.
- 610 Porco, C.C., West, R.A., Squyres, S., McEwen, A., Thomas, P., Murray, C.D., Del Genio, A., Ingersoll, A.P.,
611 Johnson, T.V., Neukum, G., Veverka, J., Dones, L., Brahic, A., Burns, J.A., Haemmerle, V., Knowles, B.,
612 Dawson, D., Roatsch, T., Beurle, K., Owen, W., 2004. Cassini Imaging Science: Instrument Character-
613 istics And Anticipated Scientific Investigations At Saturn. *Space Science Reviews* 115, 363–497.
- 614 Robbins, S.J., Antonenko, I., Kirchoff, M.R., Chapman, C.R., Fassett, C.I., Herrick, R.R., Singer, K.,
615 Zanetti, M., Lehan, C., Huang, D., Gay, P.L., 2014. The variability of crater identification among expert
616 and community crater analysts. *Icarus* 234, 109–131.
- 617 Roberts, J.H., Nimmo, F., 2008. Tidal heating and the long-term stability of a subsurface ocean on Ence-
618 ladus. *Icarus* 194, 675–689.
- 619 Schenk, P., Hamilton, D.P., Johnson, R.E., McKinnon, W.B., Paranicas, C., Schmidt, J., Showalter, M.R.,
620 2011. Plasma, plumes and rings: Saturn system dynamics as recorded in global color patterns on its
621 midsize icy satellites. *Icarus* 211, 740–757.
- 622 Schenk, P., Kirchoff, M., Hoogenboom, T., Rivera-Valentín, E., 2020. The anatomy of fresh complex craters
623 on the mid-sized icy moons of Saturn and self-secondary cratering at the rayed crater Inktomi (Rhea).
624 *Maps* 55, 2440–2460.
- 625 Schenk, P., White, O.L., Byrne, P.K., Moore, J.M., 2018. Saturn's Other Icy Moons: Geologically Complex
626 Worlds in Their Own Right. p. 237.

- 627 Schenk, P.M., McKinnon, W.B., 2024. New global topography of Enceladus: Hypsometry, basins, spherical
628 harmonics, shell thickness, and true polar wander revisited. *Icarus* 408, 115827.
- 629 Schmedemann, N., Kneissl, T., Ivanov, B.A., Michael, G.G., Wagner, R.J., Neukum, G., Ruesch, O.,
630 Hiesinger, H., Krohn, K., Roatsch, T., Preusker, F., Sierks, H., Jaumann, R., Reddy, V., Nathues, A.,
631 Walter, S.H.G., Neesemann, A., Raymond, C.A., Russell, C.T., 2014. The cratering record, chronology
632 and surface ages of (4) Vesta in comparison to smaller asteroids and the ages of HED meteorites. *Planet.
633 Space Sci.* 103, 104–130. doi:10.1016/j.pss.2014.04.004.
- 634 Shoemaker, E.M., Wolfe, R.F., 1982. Cratering time scales for the Galilean satellites, in: *Satellites of
635 Jupiter*, pp. 277–339.
- 636 Singer, K.N., McKinnon, W.B., Gladman, B., Greenstreet, S., Bierhaus, E.B., Stern, S.A., Parker, A.H.,
637 Robbins, S.J., Schenk, P.M., Grundy, W.M., Bray, V.J., Beyer, R.A., Binzel, R.P., Weaver, H.A., Young,
638 L.A., Spencer, J.R., Kavelaars, J.J., Moore, J.M., Zangari, A.M., Olkin, C.B., Lauer, T.R., Lisse, C.M.,
639 Ennico, K., New Horizons Geology, New Horizons Surface Composition Science Theme Team, N.H.R.,
640 Teams, L., 2019. Impact craters on Pluto and Charon indicate a deficit of small Kuiper belt objects.
641 *Science* 363, 955–959.
- 642 Spencer, J.R., Pearl, J.C., Segura, M., Flasar, F.M., Mamoutkine, A., Romani, P., Buratti, B.J., Hendrix,
643 A.R., Spilker, L.J., Lopes, R.M.C., 2006. Cassini Encounters Enceladus: Background and the Discovery
644 of a South Polar Hot Spot. *Science* 311, 1401–1405.
- 645 Thomas, P.C., Tajeddine, R., Tiscareno, M.S., Burns, J.A., Joseph, J., Loredo, T.J., Helfenstein, P., Porco,
646 C., 2016. Enceladus's measured physical libration requires a global subsurface ocean. *Icarus* 264, 37–47.
- 647 Werner, S.C., 2014. Moon, Mars, Mercury: Basin formation ages and implications for the maximum surface
648 age and the migration of gaseous planets. *Earth and Planetary Science Letters* 400, 54–65.
- 649 Werner, S.C., Bultel, B., Rolf, T., 2023. Review and Revision of the Lunar Cratering Chronology-Lunar
650 Timescale Part 2. *The Planetary Science Journal* 4, 147.
- 651 Wong, E.W., Brasser, R., Werner, S.C., 2021. Early impact chronology of the icy regular satellites of the
652 outer solar system. *Icarus* 358, 114184.
- 653 Wong, E.W., Brasser, R., Werner, S.C., Kirchoff, M.R., 2023. Saturn's ancient regular satellites. *Icarus* 406,
654 115763.
- 655 Xiao, Z., Di, K., Xie, M., Yue, Z., Lin, Y., Chang, Y., Wang, Y., Luo, F., Xu, R., Ouyang, H., 2024. Impact
656 Flux on the Moon. *Space: Science and Technology* 4, 0148. doi:10.34133/space.0148.
- 657 Xu, L., Hirata, N., Miyamoto, H., 2017. Ray craters on Ganymede: Implications for cratering apex-antapex
658 asymmetry and surface modification processes. *Icarus* 295, 140–148.
- 659 Zahnle, K., Dones, L., Levison, H.F., 1998. Cratering Rates on the Galilean Satellites. *Icarus* 136, 202–222.
660 doi:10.1006/icar.1998.6015.
- 661 Zahnle, K., Schenk, P., Levison, H., Dones, L., 2003. Cratering rates in the outer Solar System. *Icarus* 163,
662 263–289.

- 663 Zahnle, K., Schenk, P., Sobieszczyk, S., Dones, L., Levison, H.F., 2001. Differential Cratering of Syn-
664 chronously Rotating Satellites by Ecliptic Comets. *Icarus* 153, 111–129.
- 665 Ćuk, M., Dones, L., Nesvorný, D., 2016. Dynamical Evidence for a Late Formation of Saturn’s Moons.
666 *The Astrophysical Journal* 820, 97.
- 667 Čadek, O., Souček, O., Běhouneková, M., Choblet, G., Tobie, G., Hron, J., 2019. Long-term stability of
668 Enceladus’ uneven ice shell. *Icarus* 319, 476–484.

669 **Appendix A. Additional figures and data**

670 Appendix: Figs. A.1 to A.4.

671 **In the figure caption, some description perhaps could be adapted to the main paper or result?**

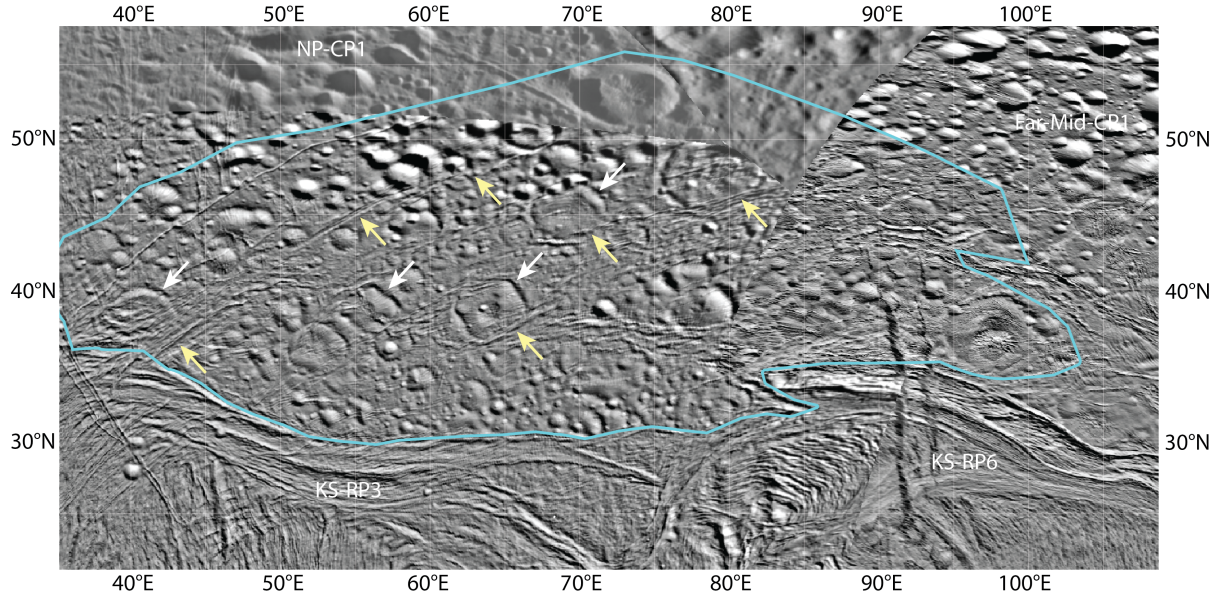


Figure A.1: CW-T-square (70°E , 40°N), also known as the Subdued Cratered Plains (Crow-Willard and Pappalardo, 2015), is one of Enceladus' most heavily cratered region. The craters here have undergone significant modification. Several large ~ 20 km craters (marked by white arrows) eroded to be shallower and more angular, likely due to relaxation from elevated heat flow (Bland et al., 2012) or tectonic deformation extending from the south-adjacent KS-RP3. The square-ish craters, influenced by pre-existing faults/troughs (e.g., Meteor Crater in Arizona (Kumar & Kring, 2008)) or subsequent tectonics, are further evidence of deformation along NE-SW troughs (yellow arrows). As a result of extensive resurfacing, the crater size-frequency measurement rolls off at ~ 10 km, in contrast to units with comparable crater densities, where it begins at ≤ 4 km.

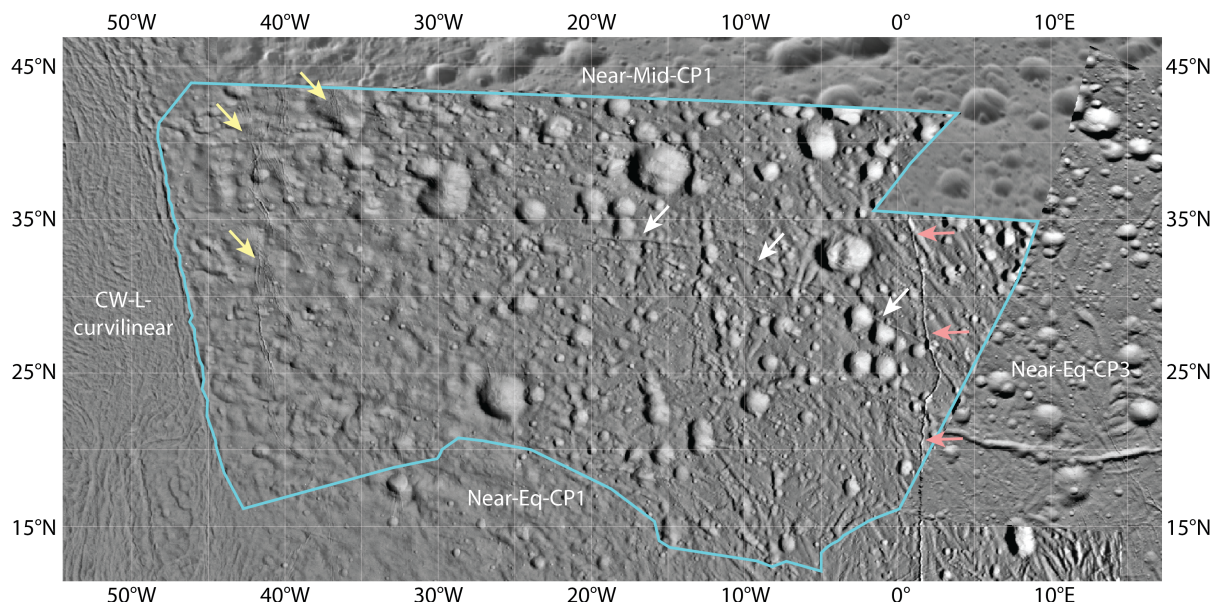


Figure A.2: Near-Mid-CP2 (20°W , 30°N), several tectonic features are evident. (i) Isolated ridges, up to 2 km wide, are scattered across the right region with varying orientations, including horizontal and NW-SE. Some ridges appear truncated by craters (yellow arrow), indicating the craters are younger, though higher-resolution images are needed to confirm this. (ii) In the western region, tectonic activity from CW-L-Curvilinear unit has transitioned into this more heavily cratered Near-Mid-CP2, where craters gradually smooth out and lose their rim and bowl shapes. (iii) The western boundary also shows pit chains cutting through these partially eroded, smooth craters (white lines). (iv) A 1 km-wide trough, extending ~ 340 km from 40°N to 37°S , cuts through ridges and craters (yellow arrows).

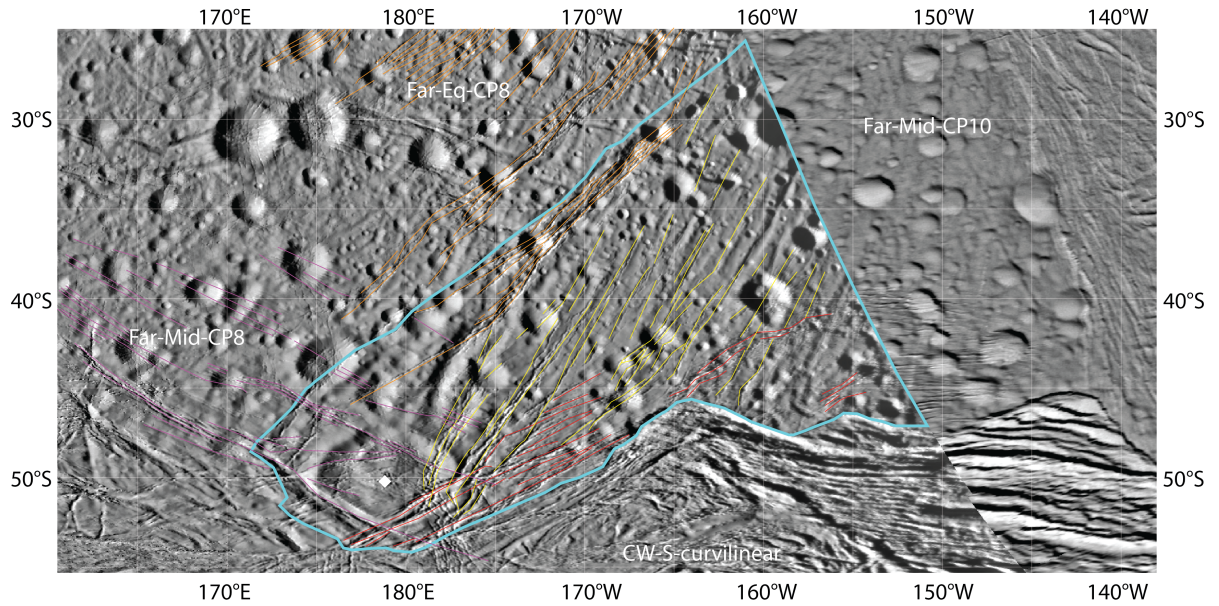


Figure A.3: Far-Mid-CP9 (165°W , 40°N) features three sets of pit chains formed at different times (Martin and Kattenhorn, 2014). The oldest NW-SE-trending chains (labelled as magenta lines) cross from the west, sharing an origin with those from Far-Mid-CP8. Two NE-SW trending chains lie along the southeast boundary adjacent to CW-S-curvilinear (red lines) and the northwest boundary adjacent to Far-Eq-CP8 (orange lines). The newest, also NE-SW chains dominate the terrain (yellow lines), intersecting most craters. The pit chain colours follow those used by Martin and Kattenhorn (2014). Due to images' resolution limits, they indicate the general direction and rough location of each branch, rather than the precise position of individual pit chains. A most obvious feature is a 22 km crater at the southwest tip (white diamond), where pit chains and ridged belts have eroded at least one-third of its rim. Craters appear progressively more eroded and smoother toward the south.

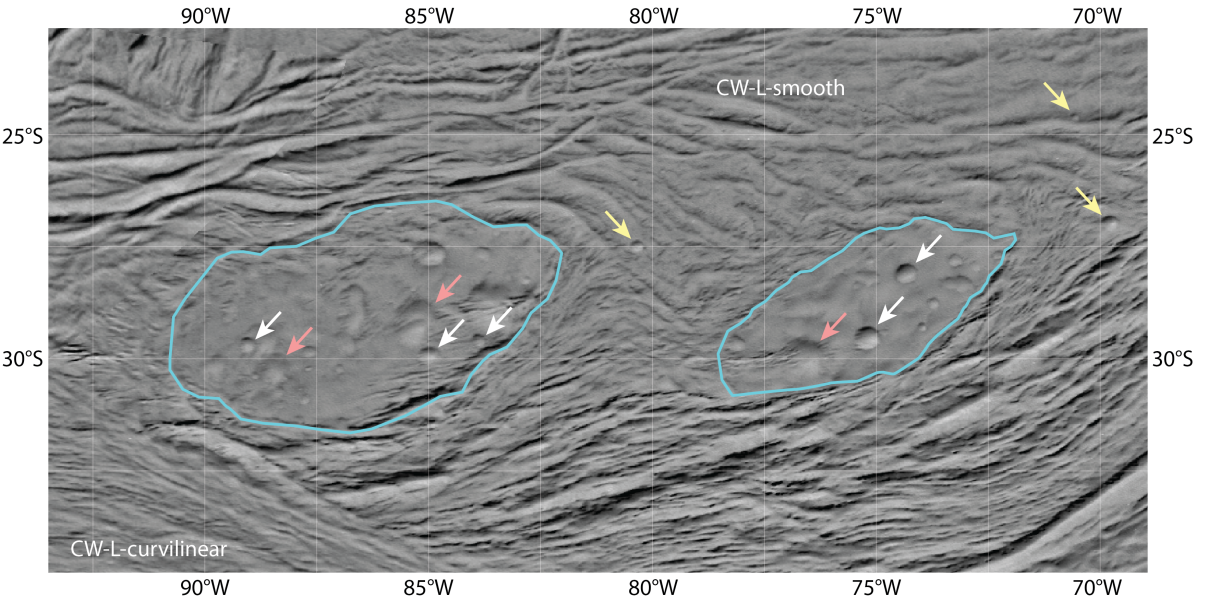


Figure A.4: CW-L-CP-island (86°W , 29°S and 75°W , 28°S) consists of two small and heavily cratered “islands” surrounded by smoother terrain (CW-L-central). Most craters (up to ~ 4 km) exhibit significant erosion, with distorted rims and shallow floors. In contrast, a few fresher craters (1.5–2 km) with clear circular rims stand out, matching the morphology of craters on the younger CW-L-central. These fresher craters likely formed after the resurfacing event that shaped CW-L-central, underscoring the erosion of pre-existing craters. The crater density here aligns with other cratered plains at similar altitudes on both the anti-Saturn side and Saturn-facing side, suggesting a once higher global crater density on Enceladus before resurfacing events like the formation of CW-L-curvilinear and CW-L-central. These relict “islands” survived the resurfacing events and preserved pre-existing craters, which can still be distinguishable.